Journal of
Materials Chemistry C

Materials for optical, magnetic and electronic devices

Accepted Manuscript

This article can be cited before page numbers have been issued, to do this please use: M. Abdollahi and M. Bagheri Tagani, *J. Mater. Chem. C*, 2020, DOI: 10.1039/D0TC03147J.

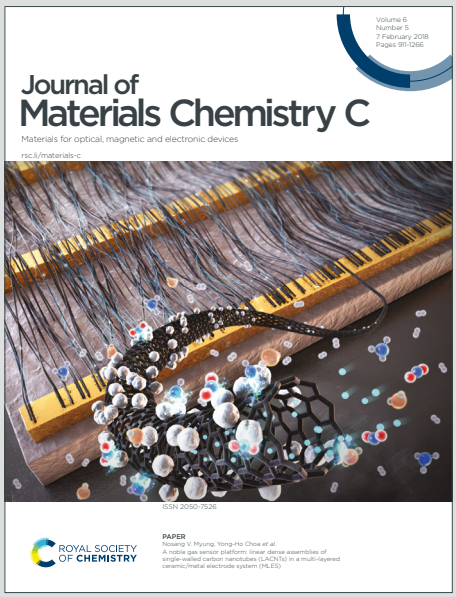

ROYAL SOCIETY OF CHEMISTRY

rsc.li/materials-c

View Article Online
DOI: 10.1039/D0TC03147J

Journal Name

ARTICLE TYPE

Cite this: DOI: 00.0000/xxxxxxxxxx

Tuning intrinsic ferromagnetic and anisotropic properties of Janus VSeS monolayer†

Mahsa Abdollahi[a] and Meysam Bagheri Tagani*[a]

Received Date
Accepted Date

DOI: 00.0000/xxxxxxxxxx

Motivated by intrinsic ferromagnetic properties and high Curie temperature of V-based Janus dichalcogenides monolayers as a new class of 2D materials, we investigated the structural, electronic and magnetic properties of the Janus VSeS monolayer by first-principles calculations. By focusing on the 2H phase which is energetically more favorable than the 1T phase, we show that the spin orientation has a profound effect on the dynamical stability and electronic structure of the VSeS monolayer. Transition from non-magnetic to magnetic phase opens a band gap and switching from anti-ferromagnetic (AFM) to ferromagnetic (FM) phase eliminates imaginary modes of phonon dispersion and stabilizes the monolayer. Magnetic and anisotropic phase diagrams of the ferromagnetic VSeS monolayer is also studied under applying biaxial strain. Tensile strain enhances the FM coupling by modifying through-bond and through-space interactions. Magnetic anisotropy energy is tunable by charge doping and a small carrier concentration can induce a transition from a ferromagnetic semiconductor to a half-metal. Moreover, by means of 2D XY model, we estimate that Berezinskii–Kosterlitz–Thouless (BKT) transition to a quasi-long-range ordered phase occurs at 83 K. We also simulate a vertical van der Waals heterostructure of VSeS/hBN to study not only the magnetic proximity effect, but also magnetic properties of VSeS monolayer on a substrate. Results indicate that the heterostructure is a ferromagnetic semiconductor and the VSeS monolayer preserves its magnetic properties, demonstrating a high potential for application in spintronics.

1 INTRODUCTION

Magnetism, originating from the spin and charge degree of freedom of electrons, has widespread applications in various fields including medical diagnosis and treatment, information storage, transportation and processing[1,2]. Recently, magnetic materials with reduced dimensionality have attracted considerable attention, so that design or discovery of two-dimensional (2D) magnetic materials paves the way towards the development of flexible spintronic devices[3–5]. According to the Mermin-Wanger-Hohenberg theorem[6], when there is no constraint on the direction of the spins (isotropic Heisenberg model), thermal fluctuation destroys the long-range magnetic order of 2D crystals at finite temperature. Therefore, for a long time, magnetism was not believed to be preserved in reduced dimensionality and access to such thin crystals, which have intrinsic magnetic properties, was an elusive dream in experimental work. But recent studies have shown that magnetic anisotropy opens a gap in the spin-wave spectrum and suppresses the effect of thermal fluctuations, consequently magnetic anisotropy preserves long-range magnetic order in the 2D crystals[7,8]. Indeed, when a material has an intrinsic anisotropy caused by spin-orbit coupling, its magnetism is also preserved in the monolayer limit[9,10]. Observation of long-range magnetic order arises from the spin-orbit coupling and other effects including magneto-static dipole-dipole interaction in pristine monolayer CrI_3 was reported[11,12]. Also a small anisotropy induced in bilayer of $Cr_2Ge_2Te_6$ at critical temperature, which caused by applying a very small magnetic field (B = 0.065T), was also reported[7]. The first report of long-range magnetic order within the CrI_3 monolayer and $Cr_2Ge_2Te_6$ bilayer appeared in 2017, with a Curie temperature (T_C) of 45 K and 28 K, respectively. Magnetic properties of these compounds can be tuned by modifying the crystal structure, the number of layers, applying gate voltage and magnetic field[7,13–16]. Since most Cr-based transition-metal trihalides are prepared by mechanical exfoliation, and they have low Curie temperatures, synthesis of 2D magnetic magnets with high performance at room temperature is a challenge for advances in spintronics applications.

[a] Computational Nanophysics Laboratory (CNL), Department of physics, University of Guilan, P. O. Box 41335-1914, Rasht, Iran.
* Corresponding Author, Email: m_bagheri@guilan.ac.ir

† Electronic Supplementary Information (ESI) available: [details of any supplementary information available should be included here]. See DOI: 00.0000/00000000.

View Article Online
DOI: 10.1039/D0TC03147J

The unique electronic and mechanical properties of 2D transition metal dichalcogenides (TMDs) including strong spin-orbit coupling effect make them promising candidates for electronic, spintronic, valleytronic and optoelectronic[17–19]. TMDs in their bulk form display a range of properties including metallic, semiconductor, superconducting states, and charge density wave (CDW) phase with the exception of ferromagnetic properties. Recent experimental advances have led to improvements in the synthesis of ferromagnetic 2D TMDs such as $MnSe_2$[20], VTe_2[21] and VSe_2[22] at room temperature. Depending on the metal atom, bulk TMDs has at least five polymorphs including: 2H, 3R, 1T, 1T′ and 1T″. Since 1T″ phase showed the lowest thermodynamic stability compared to the other phases and its layered bulk has not been reported yet, it is considered less relevant by researchers[23–25]. Due to the out-of-plane mirror symmetry in TMDs that limits the spin degrees of freedom, many attempts have been made in recent years to break this symmetry by applying electric field[26,27] and changing the structural arrangement of non-polar systems to polar systems with replacement of third element into the structural arrangement of TMDs[28]. The mirror asymmetry in the Janus structures of TMDs provides more attractive properties for application in electronics and spintronics. Although these structures are not found in nature, Lu et al. reported the synthesis of Janus MoSeS by CVD method in 2017[29]. Janus monolayer based on W and Mo transition metal atoms are intrinsic non-magnetic, but if the Janus monolayers of TMDs contain Cr, Mn, or V atoms, they show intrinsic ferromagnetic properties with high spin polarization and high Curie temperatures[30].

In laboratory, VX_2 (X: S, Se, Te) in the bulk and monolayer form generally crystallizes in the 1T polymorph with hexagonal lattice and its metallic states confirm with CDW transition[21,22,31,32]. But according to density functional theory, including on-site Hubbard-U term in calculations strongly affects the most stable phase of VX_2[33], also, the transitions between the phases may also occur using an external strain[34] and carrier doping[35]. Since the formation energy of the metallic 1T- VX_2 phase is lower than that of the semiconducting 2H-VX_2 phase, the 2H phase is more interested in theoretical calculations[36]. It is also important to remark that there is also a controversy, regarding the magnetic ground state of the VSe_2 monolayer. According to previous experimental and theoretical considerations, the VSe_2 monolayer has a magnetic order that contradicts the paramagnetic nature of VSe_2 bulk[37]. Recent studies have stated that 1T and 2H polymorphs of nonmagnetic VSe_2 monolayer are unstable, Peierls-type distortion and NM-CDW phase transition, are the origin of imaginary phonon modes of spin-restricted in 1T- and 2H-VSe2 phase, respectively[33]. Indeed, contrary to previous predictions there is a competition between the CDW phase and the magnetic order of the VSe_2 monolayer and the CDW distortion may reduce the energy of the perfect system, as a result the non-magnetic CDW state is ground state in the VSe_2 monolayer[38]. Since the VSe_2 monolayer has a large magnetic order and magnetic moment above room temperature, it can be an attractive material for van der Waals spintronics applications. The effect of graphene and MoS_2 substrates on the magnetic properties has previously been studied both experimentally and computationally[22,39,40], but the effect of hBN encapsulation on the intrinsic magnetic properties of VSe_2 and its Janus has not yet been analyzed that it would be interesting to investigate these effects on the magnetism of VSeS monolayer. Also, inspired by the dependence of intrinsic magnetic properties of the binary VX_2 by strain tuning and carrier doping[34,35,41], we will be conducting a thorough investigation into carrier doping- and strain-dependent magnetic properties of the Janus VSeS monolayer.

In this work, we first discuss the structural properties of the Janus VSeS monolayer in two 2H and 1T phases by using first-principles calculations, and then, considering that 2H phase is more stable energically, we focus on this phase to investigate the dynamic and electronic properties of the VSeS Janus in different magnetic configuration. Furthermore, we study magnetic properties of the 2H-VSeS monolayer under biaxial strain and charge doping. The ferromagnetism caused by strong through-bond interaction in the Janus VSeS is a stable state similar to the binary VS_2 and VSe_2 magnetic monolayers. According to the XY model, we obtain Berezinskii-Kosterlitz-Thouless (BKT) temperature of 82 K in the VSeS magnet. Our results show in-plane to out-of-plane easy-axis magnetic anisotropy transition under specific compressive strain of 6% and also for high concentrations of charge doping. In addition, the effect of the hBN substrate as a capsule layer is investigated. The results demonstrate that the VSeS monolayer preserves its magnetic order in the VSeS/hBN van der Waals vertical heterostructure.

2 COMPUTATIONAL METHODS

All DFT calculations were carried out using SIESTA package[42]. The PBE-GGA exchange-correlation and the Troullier–Martins norm-conserving pseudopotentials were used to describe electron-ion interactions[43]. The criteria of energy and atom force convergence were 10^{-6} and 10^{-3} eV/Å, respectively. Brillouin-zone is integrated using $15 \times 15 \times 1$ Monkhorst-Pack K-point mesh. The energy cutoff for wave functions was set to 200 Hartree and a vacuum layer of more than 20 is used to simulate the isolated sheet. To describe 3d localized orbitals of transition metal atom, we investigated the dependence of results to Hubbard U term (U=1, 2 eV). Phonon calculations are performed using a finite difference method. A $5 \times 5 \times 1$ supercell was used to calculate the dynamical matrix. In these calculations, non-magnetic (NM), ferromagnetic (FM) and anti-ferromagnetic (AFM) arrangements were considered to study spin-phonon interaction. To calculate the magnetism anisotropy energy (MAE), the spin-orbit (SO) coupling and non-collinear magnetism were included within self-consistent calculations. The MAE is defined as the difference between energies corresponding to the magnetization in the in-plane and out-of-plane directions: $E(001) - E(100)$, so the positive (negative) magnitude of the parameter indicates in-plane (out-of-plane) easy-axes.

3 RESULTS AND DISCUSSION

3.1 Structural and dynamic properties

As shown in the figures 1a and S1a (see ESI†), trigonal prismatic (D_{3h}) and octahedral (D_{3d}) coordinates of Janus VSeS monolayer has three types of atoms in the unit cell. The obtained lattice constant for two (D_{3h}) and (D_{3d}) coordinates are 3.24 (see Table 1), that is consistent with recent report[44,45]. The lattice constant for this structure is smaller than that of VSe_2 monolayer, but larger than the reported lattice constant for the VS_2 monolayer[45,46], that was expected because of the atomic radius of chalcogen atoms ($r_{Se} > r_S$). Table 1 shows the results using Hubbard term in the calculations, based on method first introduced by Dudarev et al. to describe fully-correlated electrons in half filled d-orbitals[47]. According to the Table 1, the lattice constant in 1T-VSeS is very sensitive to the changes in Hubbard term[33] and the lattice constant of 1T-VSeS is in good agreement with experimental value report for 1T-VSe_2 ($3.35 \pm 1\%$)[48] when taking into account Hubbard correction. Also, the bond length was obtained about 2.50

View Article Online
DOI: 10.1039/D0TC03147J

Table 1 Structural parameters and magnetic moment of Janus VSeS monolayer with and without Hubbard parameters (U= 0, 1, 2 eV): lattice constant, bond length of V-S (d_{V-S}) and V-Se (d_{V-Se}), vertical distance S-Se (Δ_{S-Se}), vertical distance V-Se (Δ_{V-Se}), vertical distance V-S (Δ_{V-S}), bond angle (θ_{S-V-Se}), total energy difference between the AFM and FM phases (E_{AFM}-E_{FM}), and magnetic moment of V atom.

polytypes	GGA	a (Å)	d_{V-S} (Å)	d_{V-Se} (Å)	Δ_{S-Se} (Å)	Δ_{V-Se} (Å)	Δ_{V-S} (Å)	θ_{S-V-Se} (deg)	$E_{AFM}-E_{FM}$ (meV)	magnetic moment (μ_B)
2H-VSeS	+U(0 eV)	3.241	2.366	2.515	3.126	1.68	1.446	79.610	257.49	1.16
	+U(1 eV)	3.248	2.371	2.515	3.128	1.677	1.451	79.546	266.78	1.17
	+U(2 eV)	3.256	2.377	2.52	3.133	1.678	1.455	79.499	277.6	1.18
1T-VSeS	+U(0 eV)	3.241	2.356	2.505	3.617	1.665	1.430	96.135	101.86	0.78
	+U(1 eV)	3.303	2.375	2.538	3.054	1.667	1.386	94.748	146.76	0.97
	+U(2 eV)	3.326	2.368	2.532	3.024	1.644	1.38	94.295	156.19	1.05

Table 2 Total energy difference between ferromagnetic phase of the 2H and 1T polytypes (E_{1T}-E_{2H}) of Janus VSeS monolayer with and without Hubbard parameters (U= 0, 1, 2 eV).

GGA	+U (0eV)	+U (1eV)	+U (2eV)
ΔE= E_{1T}-E_{2H} (meV)	93.12	147.53	181.44

and 2.36 in 1T-VSeS and 2H-VSeS monolayers, respectively, consistent with the theoretical values for binary VSe_2 and VS_2 presented in Ref.[46]. The total energy difference between the two 2H and 1T phases ($E_{1T}-E_{2H}$) (Table 2) shows that the 2H phase is more energetically stable in the VSeS monolayer[44,45], so hereafter, we will mainly focus on the magnetic and electronic properties of 2H phase.

In table S1 we compare VXY monolayers (X, Y=S, Se) to elucidate the impact of space symmetry breaking in the structural properties of V-based TMD monolayers. From S to Se we are faced with an increase of 2.5% in the lattice constant. The angle of X-V-Y is also dependent on the radius of the chalgogen atom so that it is enhanced from 78.8 to 79.9 when S atom is substituted with Se atom. The VS_2 and VSe_2 monolayers belong to D_{3h} point group while VSeS monolayer shows C_{3v} point group. The magnetization of V atom is also dependent on the its environment so that it is increased from $1.15\mu_B$ to $1.25\mu_B$. The difference between electron negativity of S and Se atoms leads to the change of local magnetization.

Figure 2 in supplementary demonstrates the dependence of the average potential and charge density difference on the chalcogen atom. For VS_2 and VSe_2 monolayers, the potential and charge density is symmetry around the V atom. The magnitude of the potential is dependent on the chalcogen atom so that it is higher for Se atom due to more electron negativity. Electron difference density is also symmetric around the plane of V atoms. In Janus monolayer, the potential and charge density are asymmetric. The asymmetry leads to a built-in electric field and so the piezoelectric effect in the monolayer. The asymmetry in the charge difference density can also lead to the change of the magnetic moments of the atoms and the response of the monolayer to an external electric field.

Structural stability of monolayer VSeS is investigated by calculating phonon dispersion spectrum. To emphasize the importance of the spin in the stability of the sheet, phonon band structure is computed for FM and non-magnetic sheet. Results indicate that the FM monolayer VSeS is dynamically stable, because there is no imaginary phonon mode as shown in Fig. 2. There is a band gap between acoustical and optical phonon modes, resulting in the reduction of phonon scattering and as a result, higher thermal conductivity of the sheet. Unlike other 2D materials, the flexural mode, out of plane mode, behaves linearly in the proximity of the Γ point as shown in the inset. Unlike FM sheet, the non-magnetic monolayer is unstable due to imaginary phonon mode shown in the Fig. S3, ESI†. Recently, Ref.[38] showed that the magnetism of monolayer VSe_2 can be quenched by CDW.

To elucidate the role of spin-phonon interaction in the stability of the sheet, the phonon band structure for AFM phase is also shown in Fig. 2b. There is a small imaginary mode around Γ point, indicating that the spin orientation has an important role in the stability of the sheet. In addition, there is red shift in the frequency of phonon modes in transition from FM to AFM phase. The shift is more pronounced in higher energies. We expect that the difference between phases in experiments can be revealed by Raman spectrum shift. It was theoretically predicted that the different magnetic orders in CrI_3 leads to different Raman peaks[49]. Recently, inelastic Raman spectroscopy confirmed the dependence of the Raman shift to the magnetic order of the CrI_3 monolayer[50]. However, we expect that the Raman shift should be less pronounced because of less mass difference between atoms in VSeS than CrI_3.

3.2 Electronic and magnetic properties

The spin-polarized band structure of 2H-VSeS monolayer in Fig. 1c and d shows that the monolayer is a magnetic semiconductor with an indirect energy gap of 0.16 eV, which is consistent with the results presented in the Ref.[44]. Already, the semiconductor properties of 2H-VSe_2 and 2H-VS_2 were reported with an energy gap of 0.22 eV and 0.05 eV, respectively[41]. Indeed, the band gap in these polymorphs depends on the atomic charge of the chalcogen atom, due to the electron charge transfer from chalcogen atoms, so that the energy gap in a group of chalcogen atoms decreases with decreasing electronegativity from top to bottom. Therefore, as expected, the energy gap of the VSeS monolayer is larger than that of VS_2 and smaller than that of VSe_2. Also, it is remarkable that the values of spin-up and -down gaps were 0.667 eV and 0.547 eV, respectively. By including the Hubbard term (U = 2 eV), the value of spin-up gap is decreased to 0.646 eV and the spin-down gap is increased to 0.58 eV (Fig. S5a and b, ESI†). It is noteworthy that FM order of 2H-VSeS monolayer has caused the metal-semiconductor phase transition (Fig. S4a, ESI†). Also due to the Supplementary Fig. S5b (see ESI†), 2H-VSeS has metallic behavior in the AFM spin configuration. 1T-VSeS shows metallic behavior (Fig. S1c, ESI†), which is consistent with the results using PBE and HSE functional in[44]. Also, the ferromagnetic metallic state of the 1T-VSe_2 and 1T-VS_2 monolayers have already been demonstrated[34,51,52].

According to spin-resolved density of states around the Fermi energy in Supplementary Fig. 5, obviously the metal atom has the main contribution in the valence band maximum (VBM) and

View Article Online
DOI: 10.1039/D0TC03147J

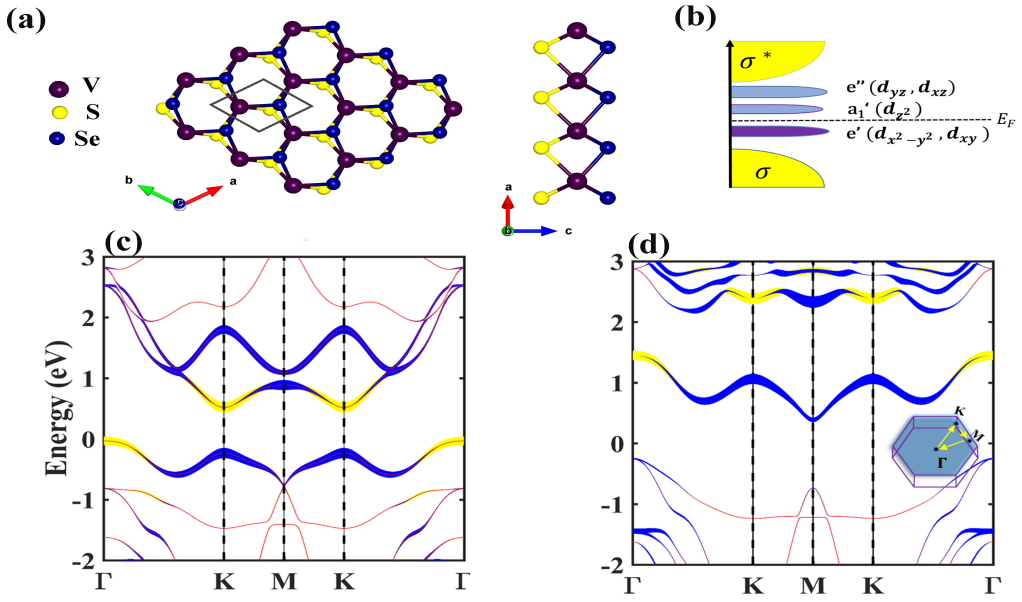

Fig. 1 Top and side view of (a) Janus 2H-VSeS monolayer with trigonal prismatic coordinate. The vanadium, selenide, and sulfur atoms are shown in purple, blue, and yellow, respectively. Unit cell is also identified. (b) Schematic illustration of energy splitting and crystal field. (c) The spin-polarized band structure of 2H-VSeS. The spin-up and spin-down band structures demonstrate with (c) and (d), respectively. Yellow circles denote contributions from the vanadium a_1' (d_{z^2}) orbital, while blue circles are for e' ($d_{x^2-y^2}$, d_{xy}) orbitals. The inset in (d) shows the Brillouin zone. Fermi level is set to zero.

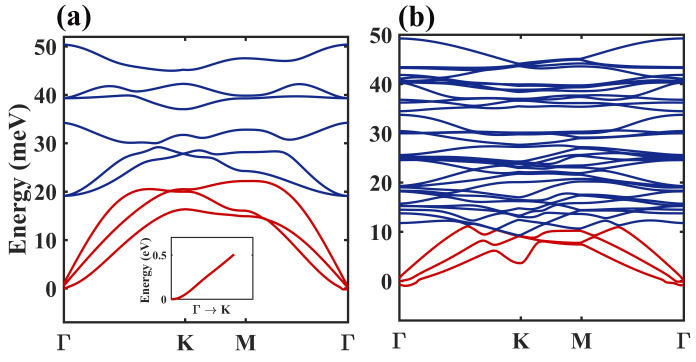

Fig. 2 Phonon band structure of VSeS monolayer for (a) FM and (b) AFM phase. Blue (red) lines indicate optical (acoustic) phonon modes. The behavior of out-of-plane mode around Γ point is shown in the inset.

conduction band minimum (CBM). Indeed, metal atom states are responsible for ferromagnetism in the VSeS monolayer. Distribution of vanadium atom states is less in above Fermi energy and sharper peaks in density of states are observed in this range of energy. The localized states of V-d, S-p and Se-p orbitals near the Fermi energy in projected density of state (Fig. S6b and d, ESI†) show the hybridization between these orbitals due to the covalent-like bonds. Spin splitting of S atom orbitals is greater than that of Se atom, which indicates a strong interaction between the V-d and S-p orbitals.

By considering two FM and AFM spin configuration for the VSeS monolayer, we show that the VSeS monolayer similar to binary VS_2 and VSe_2 has a magnetic order. Comparing the total energy of two FM and AFM arrangements in a $2\times2\times1$ supercell (see Table 1) shows that the ground state of VSeS monolayer is ferromagnetic in agreement with reported result in [30,44,45]. As seen in the Table 1, magnetic moment of V atom is $1.16\mu_B$ for 2H-VSeS, without taking into account the Hubbard term. In 2H phase with trigonal-prismatic coordinates, d orbital of V atom breaks into three degenerate groups in crystal field splitting: a' (d_{z^2}), e' ($d_{x^2-y^2}$,d_{xy}) and e'' (d_{yz},d_{xz}) (see Fig. 1b). The a' (d_{z^2}), e' ($d_{x^2-y^2}$,d_{xy}) orbitals have the lowest energy levels [17,48,53], also minority and majority spins are completely separated (Fig. 1c and d), so the $3d^1$ electron completely fills the one of the two spin states and as a result, the magnetic moment becomes $\sim1\mu_B$. As shown in Figure 1c and d, a d-orbital in the majority spin channel is filled with one electron of V^{4+} ion and the five minority spin channels and empty majority channels are located above the Fermi energy. Exchange splitting has created the spin gap in two minority- and majority-spin band structures. Also the magnetic moment of 1T-VSeS was obtained to be $0.78\mu_B$. Indeed, the crystal field in octahedral coordinates breaks the 3d orbitals of V atom to triplet degenerate states t_{2g} (d_{xy}, d_{xz}, d_{yz}) and doublet degenerate states e_g ($d_{x^2-y^2}$, d_{z^2}) (see Fig. S1b, ESI†). According to Supplementary Fig. 1, the t_{2g} state of the majority and minority spin cross the Fermi level, so the electron of the last layer in the V atom partially fills the two spin-polarized bands and it causes the magnetic moment to be half-integer and smaller than $1\mu_B$ in ferromagnetic metal 1T-VSeS.

Obviously, the interaction between highly localized electrons affects the magnetic properties of the VSeS monolayer and increases the magnetic moment and energy difference between the ferromagnetic and antiferomagnetic states in both 1T and 2H phases. This behavior has already been seen in the VS_2 and VSe_2 monolayers using the density function theory [18,51]. Indeed, by applying Hubbard term, the energy gap of the 2H-VSeS increases (Supplementary Fig. 4a and b, ESI†), as a result, more electrons are located in the majority spin of the valence band and magnetic moment increases. In the 1T-VSeS monolayer for U = 1, 2 eV, the majority spin is moved below the Fermi level (Supplementary Fig. 3c and d, ESI†) and the t_{2g} state is completely polarized, so as expected, the obtained magnetic momentum of the V atom is $\sim1\mu_B$ (Table 1). In [41], this change in energy and magnetism has been related to contributions of the DFT energy, the filling and ordering

View Article Online
DOI: 10.1039/D0TC03147J

of V-d orbitals energy in DFT + U energy functional. According to the results provided in[41], we predict that for sufficiently high values of U, 1T phase becomes the magnetic ground state.

Usually two magnetic interactions compete with each other in the monolayers: direct and indirect exchange interactions. According to the Kanamori-Anderson rule[54,55], super-exchange of 2H-VSeS monolayer with bond-angle (θ_{S-V-Se}) of 90^0 at the next near-neighbor is always ferromagnetic and there is a direct-exchange interaction (AFM arrangement) between the single electron at the e'-like state with the other e'-like states of V atom as the near-neighbor, that due to the small overlap between these states, FM interaction overcomes to AFM interaction. In 1T-VSeS monolayer, octahedral environment bringing the atoms closer together and overlap of the t_{2g} orbitals becomes stronger compared to the 2H-VSeS, as a result, the energy difference between the FM and AFM actually decreases (Table 1), but still indirect ferromagnetic interaction is the main mechanism in the exchange interaction of 1T phase. It is noteworthy that, recently, due to the lack of spin splitting in band structure of 1T-VSe_2 (unlike DFT predictions) using angle-resolved photoemission spectroscopy (ARPES), Cohelho et al. realized the importance of stable competing states, including CDW mode, to determine the characteristics of this class of materials[38]. We will also show that the Janus 2H-VSeS structure may not be an itinerant ferromagnetic and there may be a competition between the non-magnetic CDW phase and the ferromagnetic phase.

The spin Hamiltonian of the ground state of the monolayer can be described by a Heisenberg model, including single ion anisotropy to describe the magnetic behavior of the system as[56]:

$$H = -1/2 \sum_{<i,j>} [J^x S_i^x S_j^x + J^y S_i^y S_j^y + J^z S_i^z S_j^z] - \sum_i D(S_i^z)^2, \qquad (1)$$

where the sum over i runs over the entire lattice of V atoms, and $< i, j >$ denotes nearest neighbors of V atoms. J^α with α={x,y,z} denotes the anisotropic spin-exchange interaction energy, and D describes single ion magnetic anisotropy. $J^\alpha > 0$ favors ferromagnetic interactions, and $D > 0$ favors off-plane easy axis. The spin-exchange interaction energy can be computed using non-collinear calculation and including ferromagnetic and antiferromagnetic interaction in a 2×2 supercell as:

$$J^\alpha = \frac{E^\alpha_{AFM} - E^\alpha_{FM}}{16S^2}, \qquad (2)$$

where S=1/2 for monolayer VSeS and $E^\alpha_{FM(AFM)}$ denotes parallel (anti-parallel) spin orientation along α direction. Our results demonstrate that the J^α are isotropic so that the minimal Hamiltonian that can be used to capture the magnetism of the monolayer is:

$$H = -(1/2J \sum_{<i,j>} \vec{S}_i.\vec{S}_j + D\sum_i (S_i^z)^2). \qquad (3)$$

Magnetic anisotropy energy (MAE) is dependent on the spin-orbit coupling and composed of magneto crystalline anisotropy, and of dipole-dipole interaction as magnetic shape anisotropy. In low dimensional systems, it was shown that the magneto crystalline anisotropy dominates MAE[57]. One should conduct collinear and non-collinear spin-polarized DFT calculation with taking into account SOC to compute magnetic ion anisotropy parameter as:

$$D = \frac{E^\beta_{FM} - E^z_{FM}}{4S^2}, \qquad (4)$$

where $\beta \in \{x, y\}$. The obtained values of J and D are 64 meV and -1.82 eV, indicating the in-plane magnetic anisotropy is very robust. The results demonstrate that origin of magnetism in the monolayer comes from in-plane magnetic anisotropy and it is very difficult to flip the spins along out of plane axis. In following, we show that the biaxial strain with high magnitude and doping with nearly high concentration are main mechanisms to convert the monolayer VSeS form a 2D XY ferromagnet to Ising one.

3.3 Tuning magnetism by strain and charge doping

Strain engineering is a promising method for manipulation of magnetization in vanadium dichalcogenides[34,58]. Indeed, according to previous studies, understanding the effect of strain on the magnetic properties of Janus TMDs will be favorable. In the laboratory, methods such as suitable lattice mismatch for substrate, the difference in thermal expansion between the substrate and the 2D material film, and compression of the substrate are used to produce a wrinkled structure and induce strain. To examine the strain-dependence of magnetism, we applied a biaxial-strain according to $\varepsilon = \frac{a - a_0}{a_0} \times 100$ relation, where a_0 (a) is lattice constant of relaxed (strained) monolayer. We investigated variation of buckling height, V-S, V-Se and V-V bond length as a function of biaxial-strain variation ranged from -10% to + 10% in 2H-VSeS (Fig. 3a). With the tensile strain, the V-S, V-Se, V-V bond length and buckling height increase. Indeed, strain weakens the covalent-bond between the V atoms and the nearest-neighbor atoms. As seen, V-S and V-Se bond length shows a weak dependence to strain, unlike the buckling and V-V bond length. As buckling parameter decreases, the overlap of the $\pi - \pi$ orbitals increases and the structure be more stable. The change in energy gap is not uniform in terms of strain and occurs semiconductor-metal transition in strain greater than 7% and -4% (inset of Fig. 3a).

Figures 3b and c show the calculated magnetic moment of the V, S, and Se atoms in term of strain. As we see the V atom has a main contribution in the magnetic moment of monolayer. By applying 10% tensile strain, the magnetic moment of V, S and Se atoms increased 25%, 87% and 296%, respectively, compared to the relaxed structure. Also, all three atoms still have spin-polarization in compressive strain up to -10%. Indeed, by increasing the bond length in tensile strain, the ionic-bond interaction overcomes to the covalent-bond interaction, and as a result, the number of un-paired electrons in V atom increases leading to increase of magnetic moment. The behavior of magnetic moment in 2H-VSeS structure in rang of -5% to 5% strain is consistent with studies performed on the binary VS_2 and VSe_2 monolayers[58].

In addition, strain not only changes the magnitude of the magnetic moment, but also affects the ferromagnetic coupling of the structure by changing two parameters: (1) through-bond interaction (FM coupling) and (2) through-space interaction (AFM coupling). In vanadium- and niobium dichalcogenides monolayers[58,59], due to the localized magnetic electrons of Nb and V-3d and their small spatial distribution, indirect through-bond interactions are larger than space-through interactions, so the FM arrangement is more stable in these monolayers. According to Fig. 3d, by increasing the compressive strain to the critical point of -6%, the exchange energy ($E_{AFM} - E_{FM}$) decrease as expected but FM arrangement is still stable. In a larger compressive strain up to -10%, the exchange energy increases. By applying tensile strain and increasing the V-X and V-V bond length, both through-space and through-bond interactions become weaker. But since the increase in V-V bond length is faster than V-X bond length (Fig. 3a), reducing through-space interaction is faster than reducing through-bond

View Article Online
DOI: 10.1039/D0TC03147J

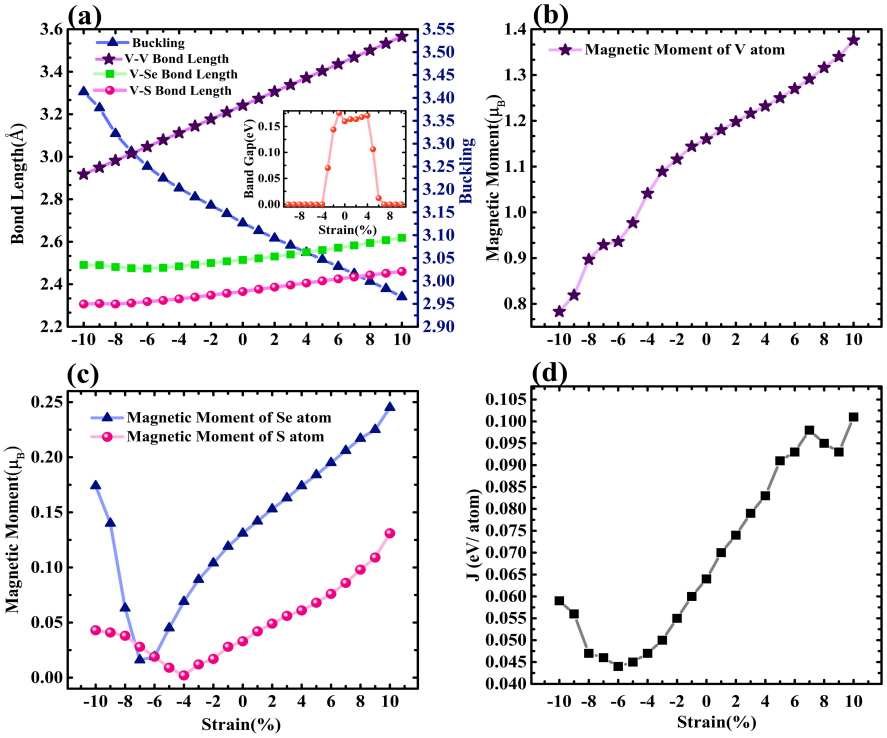

Fig. 3 (a) Variation of buckling height, V-X and V-V bond (b), (c) ferromagnetic moment and (d) exchange parameter J in terms of biaxial strain in 2H-VSeS. The inset plot in (a) is variation of band gap versus of strain.

interaction. As a result, exchange energy ($E_{AFM} - E_{FM}$) increases with increasing tensile strain and the FM phase becomes more stable. This phenomena is not unique and is dependent on the bond length, atomic arrangement, and atoms forming the structure. For example, in the half-fluorinated of graphene, GaN and BN behave different, so that by increasing tensile strain, reducing the through-bond interaction is more significant than the direct p-p interaction in magnetic atoms and the AFM phase is more stable in these structures[60].

In Fig. 4a, the magnetic anisotropy energy (MAE) of the 2H-VSeS monolayer due to the biaxial strain is shown. As mentioned in previous section, the MAE is defined as the difference between energies corresponding to the magnetization in the in-plane and out-of-plane directions: $E(001) - E(100)$, so the positive (negative) magnitude of the parameter indicates in-plane (out-of-plane) easy-axes. The high and positive MAE value (0.455 meV/atom) indicates an in-plane orientation of the magnetic moments in the Janus VSeS monolayer. In VS_2 and VSe_2 monolayers, the MAE value is reported to be 0.21 meV/atom and 0.60 meV/atom, respectively[41]. Se atom is heavier than S atom, the spin-orbit coupling strength in Se atom is more, so the value of MAE for Janus VSeS is greater than the reported MAE value for VS_2 and smaller than that for VSe_2. By applying tensile strain of about 10%, the MAE parameter increased by 185% compared to the relaxed monolayer(see Fig. 4a). Also by applying compressive strain, the MAE decreases to a critical point (-6%), after which it increases. Indeed, the in-plane to out-of-plane easy-axes transition occurs in this critical point.

To elucidate the origin of dependence of the MAE on the strain, we consider contribution of second order SOC interaction to MAE by involving occupied and unoccupied d-orbital states[61]

$$\Delta E_{ij} = \frac{|<i|H_{so}(x) - H_{so}(z)|j>|^2}{\varepsilon_j - \varepsilon_i}, \tag{5}$$

where $H_{so}(\theta) = D^{\dagger}(\theta)\frac{\zeta}{2}\vec{\sigma}.\vec{L}D(\theta)$ is SOC Hamiltonian[62], D and ζ denote rotational matrix and SOC constant, respectively. In-plane or out-of-plane magnetization is directly related to the spin and orbital angular momentum of states $|i>$, and $|j>$. Contribution of the SOC interaction to the MAE can be classified into two parts: one involving the same spin channels and the other is dependent on the different spin channels[61,62]:

$$\Delta E_{\pm,\pm} = (\frac{\zeta}{2})^2 \frac{|<i^{\pm}|L_z|j^{\pm}> - <i^{\pm}|L_x|j^{\pm}>|^2}{\varepsilon_j - \varepsilon_i}, \tag{6a}$$

$$\Delta E_{\pm,\mp} = (\frac{\zeta}{2})^2 \frac{|<i^{\pm}|L_x|j^{\mp}> - <i^{\pm}|L_z|j^{\mp}>|^2}{\varepsilon_j - \varepsilon_i}, \tag{6b}$$

where $i^+(j^+)$ and $i^-(j^-)$ stand for occupied (unoccupied) of majority and minority spin states. The energy difference between unoccupied and occupied states are inversely proportional to the magnitude of the MAE, so the states near the Fermi level have dominant role. As it is clear from Fig. 1c the d-orbitals of V atom are responsible of the VBM and CBM. Three predominant orbitals, determining the valence and conduction bands, are d_{z^2}, $d_{x^2-y^2}$, and d_{xy}, i.e. $|2,0>$, and $|2,\pm 2>$ orbitals. For relaxed monolayer, the VBM is composed of $|d_{z^2}\uparrow>$, $|d_{x^2-y^2}\uparrow>$, and $|d_{xy}\uparrow>$, and the CBM is formed from $|d_{x^2-y^2}\downarrow>$, and $|d_{xy}\downarrow>$, see Fig. 1c. The only contribution to the MAE comes from different spin channels and the non-vanishing term is related to $<d_{x^2-y^2}|L_z|d_{xy}>$ with a negative sign, leading to the in-plane magnetic anisotropy. For tensile strain higher than 6% a transition from semiconductor to half-metal is oc-

View Article Online
DOI: 10.1039/D0TC03147J

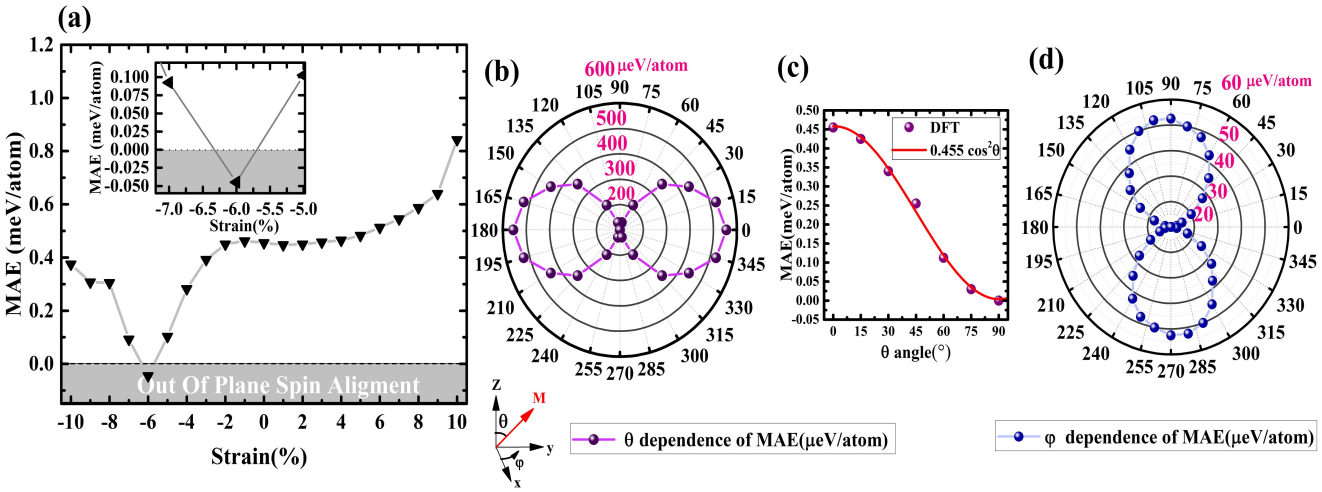

Fig. 4 (a) Dependence of magnetic anisotropy energy (MAE) on the biaxial strain. (b) Dependence of the MAE on the polar angle (θ). (c) comparison between the MAE obtained from DFT and Eq.7 as a function of θ. (d) Dependence of the MAE on the azimuth angle (φ).

curred leading to contribution of same spin channels to the MAE. In addition, $|d_{xz}\uparrow>$, and $|d_{yz}\uparrow>$ orbitals come also into play , see Fig. S7 (ESI†), and as a result, $< d_{x^2-y^2}|L_x|d_{yz} >$, and $< d_{xy}|L_x|d_{xz} >$ are now finite, giving rise to the increase of in-plane magnetic anisotropy according to Eq.6a .

The MAE reduces under compressive strain and a transition from 2D XY magnet to Ising magnet is observed at $\varepsilon = -6\%$. At this critical strain, a Dirac cone is observed for the spin-down and a band of spin-up pierce the Dirac cone as shown in Fig. S8, ESI†. Both spin channels and all d-orbitals contribute in the bands in the vicinity of the Fermi level as seen in Fig. S9 (ESI†), causing a transition in the magnetic anisotropy energy from in-plane to out-of-plane. By increase of compressive strain higher than 6%, a transition to the half-metal is observed, but here, spin-down is the majority. The unoccupied state in the vicinity of the Fermi level is composed of all d-orbitals, see Fig.S10 (see ESI†), so $< i^{\downarrow}|L_x|j^{\downarrow} >$ with negative sign dominates the MAE leading to in-plane magnetization.

Dependence of the MAE on the polar angle (θ) and azimuthal angle (φ) is also investigated in Fig. 4. For polar angle, we defined $MAE = E^{\theta}_{FM} - E^{x}_{FM}$ where $\theta = 0$ denotes spins aligned out-of-plane. The MAE oscillates with the polar angle so that its dependence on the θ can be described with :

$$MAE(\theta) = -\lambda cos^2(\theta), \qquad (7)$$

where λ is the single-site anisotropy constant and $\lambda > 0$ favors in-plane magnetization. The results obtained from DFT and Eq.7 is plotted in Fig. 4c, indicating an excellent agreement between the results with $\lambda = 0.455$meV. This angular dependence $cos^2(\theta)$ of energy was observed in perfect thin film with two-fold symmetries[57,63]. Clearly, the MAE is more weakly-dependent on the azimuth angle φ (Fig. 4d). Due to the small energy difference between the two X and Y spin orientations compared to that between two Z and X spin orientations, we conclude that there is continuous O(2) spin symmetry in the plane of VSeS monplayer. We expect that there is no spin preference for the Janus 2H-VSeS structure on the XY plane and the results on the Y-orientation are same as the results of X-orientation. So in the following, we will focus only on the X spin orientation.

It is remarkable that due to in-plan magnetism in 2H-VSSe, it can be described according to the 2D XY model[64,65]. According to the XY model, in addition to the lack of long-range transition in Curie temperature (T_C), at low temperatures below a finite temperature (BKT[65]), magnetic susceptibility diverges and a quasi-long-range magnetic order is created. Based on the obtained results through Monte Carlo, the BKT transition temperature are obtained to be 83 K in according to the $T_{BKT} = \frac{0.89}{32K_{\beta}}(E_{AFM} - E_{FM})$ relation[66]. Due to the dynamic instability of non-magnetic 2H-VSeS and fairly high BKT temperature in 2H-VSeS, we predict that phase transition from nonmagnetic to CDW phase appears and as a result we expect a competition between the non-magnetic CDW phase and magnetic ground states[33,38].

In the semiconductor industry, charge carrier doping is an effective way to tune the Fermi energy. In experiments, the charge density can be injected using an ionic liquid as a dielectric gate or surface absorption of an organic molecule[67,68]. Previously, the magnetic, semi-metallic, and valley polarity properties of the 2D SnX_2 (X: Se, S), VS_2, and VSe_2 were investigated by electron and hole doping[35,69,70]. Due to the presence of un-paired electrons in the d-orbital of Janus VSeS monolayer, it is expected that its electronic and magnetic properties will be tuned by charge carrier doping. As shown in inset of Fig. 5a, since the magnetic moment of the V atom is significantly reduced and no magnetic phase transition observed in high concentrations of the electron and hole doping, so 2H to 1T phase transition is predicted in high values of charge concentration similar to binary VS_2[35].

MAE decreases with increasing charge concentration and the easy axes are perpendicular to the plane for $> 4 \times 10^{14}\ cm^{-2}$ and $< -5 \times 10^{14}\ cm^{-2}$ concentrations (Fig. 5a). Magnetic moment decreases by 45% (37%) at the hole(electrone) doping concentration of $5 \times 10^{14}\ cm^{-2}$. Also MAE decreases by 102%(113%) at the hole(electrone) doping concentration of $5 \times 10^{14}\ cm^{-2}$. Therefore, it can be concluded that change in SOC has caused the reduction in MAE, but magnetic moment does not affect in MAE. This behavior has already been observed in Fe_3GeTe_2 monolayer[71].

Due to the relatively small energy gap in the 2H-VSeS monolayer, the system can show the phase transition to half-metal state by applying a gate voltage. Also because of the large enough value of spin exchange splitting in valence and conduction band

View Article Online
DOI: 10.1039/D0TC03147J

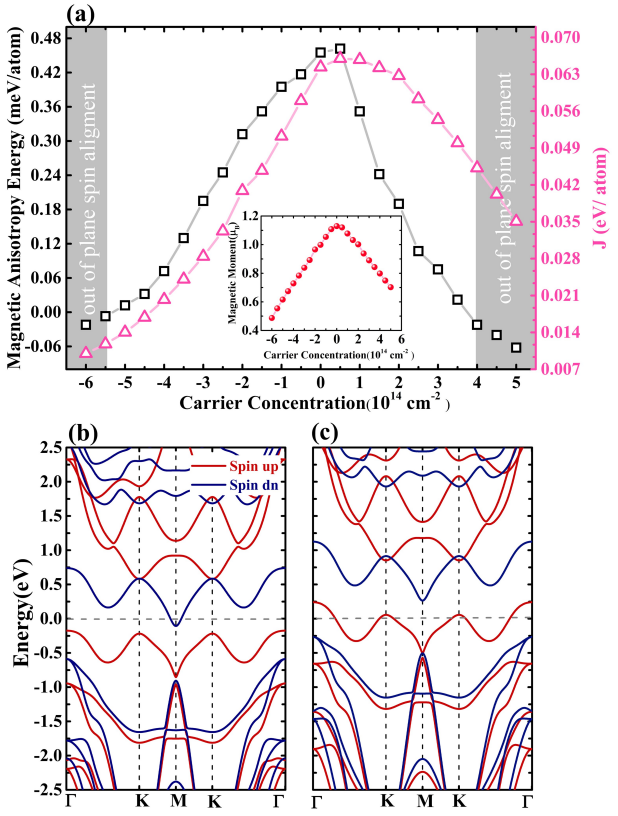

Fig. 5 (a) Dependence of MAE and exchange energy (J) on carrier concentration. (b) Electron and (c) hole doped band structure with carrier concentration of $2 \times 10^{14}\ cm^{-2}$. The inset plot in figure (a) is magnetic moment of V atom as a function of carrier concentration. The Fermi level is set to zero.

(Supplementary Fig. 6b, ESI†), the efficiency of the spin filtering will be maintained by applying the gate voltage over a wide range and it will be easier to be the experimentally controlled the semi-metallic doping properties of the structure . As shown in Fig. 5b and c, by small concentration of electron and hole ($2 \times 10^{14}\ cm^{-2}$), semiconductor/half-metal FM transition with 100% spin-polarization around Fermi energy is observed. When the type of doping change from electron to hole, the direction of the spin-polarization is inversed. This property has already been observed in bipolar magnetic semiconductors [72], that is performed by inverting the polarity of the gate voltage experimentally.

3.4 hBN/VSeS van der Waals heterostructure

Vertical van der Waals (vdW) heterostructures composed of 2D monolayers are among the most interesting structures studied in recent years due to their potential for application in future electronics and spintronics. Furthermore, proximity effects in heterostructure can induce some features in each counterpart, leading to tuning electronic properties of each layer. In experiments on magnetic layers, the magnetic layer is sandwiched between two hexagonal boron-nitride sheet (hBN) not only to protect the magnetic layer from the environmental effects, but also to control the magnetic layer under external fields in a suitable manner. In this section, we simulate a vdW heterostructure composed of hBN/VSeS monolayers to understand, first, effect of hBN sheet on the magnetic properties of VSeS, and, second, the magnetic proximity effect induced by VSeS on the hBN. We used the empirical correction method proposed by Grimme (GGA+D3) to take into account the long range van der Waals intraction between two layers [73]. A $\sqrt{7} \times \sqrt{7}$ supercell of monolayer hBN and a 2×2 supercell of VSeS monolayer is used so that the heterostructure has 26 atoms. The most stable stacking of the heterostructure is shown in Fig. 6a where a V atom is directly above one B atom and a Se atom is directly above one N atom. The lattice constant of the heterostructure is 6.62 , and the vertical distance between two layers is 3.51 that is comparable with the distance reported for CrI3/TMD heterostructures [74].

Two different spin configurations, FM and AFM, for VSeS are considered to take into account the effect of hBN substrate on the magnetization of the upper sheet. The FM state is still the ground state so that $E_{AFM} - E_{FM} =$ 0.242 eV. The substrate cannot change the preferred spin orientation of monolayer VSeS, so the heterostructure will be a magnetic composite at room temperature. Fig. 6b shows band structure of the heterostructure in the FM ground state. The spin band gap is modulated in the presence of the substrate. Spin-up (down) band gap is 0.39 eV (0.76 eV) and indirect. The VBM (CBM) for spin-up is located at Γ (K) point and Γ ($M \rightarrow \Gamma$) for spin-down, therefore the substrate changes the type of the band gap from direct to indirect for spin-down. When the magnetization of the heterostructure is in the AFM state, there is an interesting point. We find that the degeneracy between spin bands is lifted in the AFM as shown in Fig. S11a (ESI†) around the Fermi level. This can be attributed to breaking of the symmetry, and proximity effects. All bands around the Fermi level appertain to the VSeS monolayer as indicated in Fig. S11b, ESI†. The proximity effect leads to induction of magnetization in hBN sheet, so that some spin states are observed far from the Fermi level belonging to monolayer hBN as shown in Fig. S11b, ESI†.

Interlayer charge transfer of hBN/VSeS vdW heterostructure is investigated using electrostatic potential difference between layers, differential charge density, and Mulliken population analysis. We found that $2.9 \times 10^{16}\ m^{-2}$ electron is transferred from monolayer hBN to VSeS monolayer.There is a built-in potential with a height of 3.475 eV between layers, leading to induction of electric field toward the hBN sheet as shown in Fig. 6c. Therefore, electrons flow from hBN to VSeS sheet. Fig. 6c shows that the potential is asymmetric in the VSeS sheet, causing from the difference of electronegativity between Se and S atoms. Spin-dependent differential charge density projected in the axis perpendicular to the heterostructure plane is drawn in Fig. 6d. The electron difference density is defined as:

$$\delta n(\vec{r}) = n(\vec{r}) - \sum_{I}^{N} n_I(\vec{r}), \qquad (6)$$

where n_I is the charge of atom I and N is the number of the atoms in the heterostructure. Spin-up is transferred from Se and S atoms to V atom and a little charge is also transferred to the hBN sheet. In contrast, spin-down charge density is different in two sheets. The charge is tranfered from V atom to S/Se neighbor atoms and also to the hBN sheet. Indeed, the hBN sheet gains some polarized charge due to the proximity effect. Although, the net charge is transferred from the hBN sheet to monolayer VSeS, the interplay between the built-in potential and magnetic exchange effect induced by V atoms, disturbs uniform distribution of the charge on the hBN sheet, and a spin polarization is observed in the sheet.

View Article Online
DOI: 10.1039/D0TC03147J

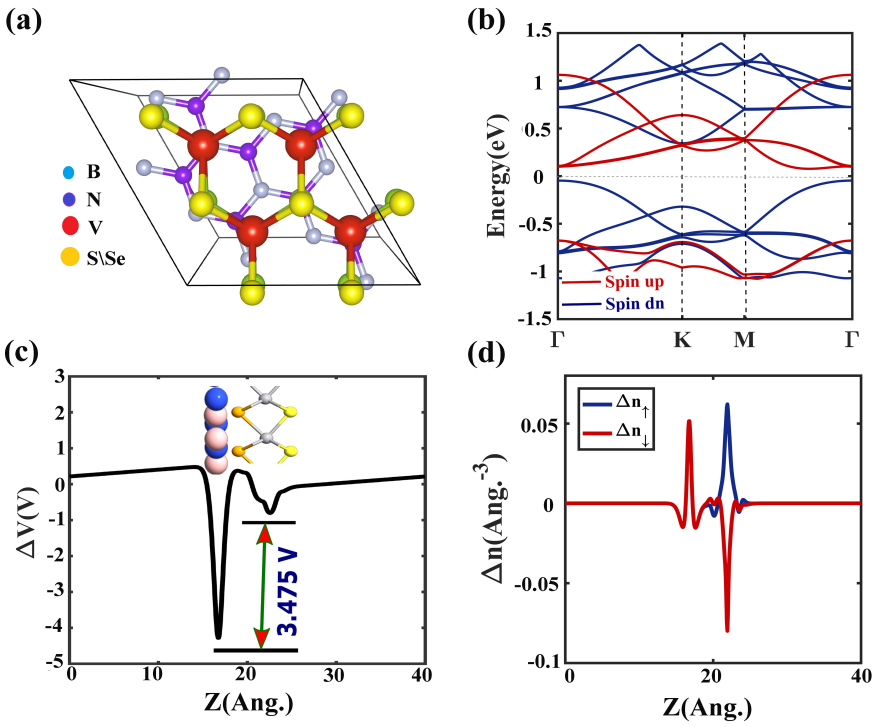

Fig. 6 (a) Top view of hBN/VSeS vdW heterostructure in the most stable stack. (b) Band strauctur of the heterostructure in FM state. (c) Electrostatic potential difference along z-direction. (d) Spin-dependent differential charge density projected along z-direction. Fermi level is set to zero.

4 CONCLUSION

In this work, we present a density functional theory (DFT) investigation on a new type of intrinsic ferromagnetic semiconductor: Janus VSeS monolayer. Comparison between total energy of two 2H and 1T phases shows that the 2H phase is more stable. Spin-lattice interaction has an important role in electronic and dynamical properties of the sheet and causes a transition from metal to semiconductor. In addition, spin-phonon interaction results in a red shift in optical phonon modes in transition from ferromagnetic (FM) to antiferomagnetic (AFM) phase. The positive and high value of magnetic anisotropy energy (MAE) indicates easy-axis of VSeS is parallel to monolayer. We demonstrated the MAE ia weakly dependent on the azimuth angle φ, so there is no long-range magnetic order for VSeS monolayer at finite temperature. We have also examined the effect of biaxial strain and carrier doping on the magnetic properties of VSeS monolayer. The stability of the FM coupling, arising from the nearly 90^0 Se-V-S exchange path, is promoted by increasing the tensile strain. Also, a transition from magnetic semiconductor to magnetic matal is happned for strains higher than 5%. A low concentration of charge doping can turn VSeS monolayer into a half-metal with 100% spin-polarization and a transition of spin easy-axis is observed for high doping concentration. Band gap and magnetic properties of monolayer VSeS can be also tuned by stacking it on h-BN monolayer via magnetic proximity coupling and charge transfer.

Conflicts of interest

There are no conflicts to declare.

Notes and references

1 H. Dery, P. Dalal, L. Sham *et al.*, *Nature*, 2007, **447**, 573–576.
2 H. Dery, H. Wu, B. Ciftcioglu, M. Huang, Y. Song, R. Kawakami, J. Shi, I. Krivorotov, I. Zutic and L. J. Sham, *IEEE Transactions on Electron Devices*, 2011, **59**, 259–262.
3 C. Tang, C. Zhang, Z. Jiang, K. Ostrikov and A. Du, *Journal of Materials Chemistry C*, 2019, **7**, 5792–5796.
4 X. Zhang, M. Zhao, A. Wang, X. Wang and A. Du, *Journal of Materials Chemistry C*, 2013, **1**, 6265–6270.
5 C. Tang, L. Zhang, S. Sanvito and A. Du, *Journal of Materials Chemistry C*, 2020, **8**, 7034–7040.
6 N. D. Mermin and H. Wagner, *Physical Review Letters*, 1966, **17**, 1133.
7 C. Gong, L. Li, Z. Li, H. Ji, A. Stern, Y. Xia, T. Cao, W. Bao, C. Wang, Y. Wang *et al.*, *Nature*, 2017, **546**, 265–269.
8 Y. Deng, Y. Yu, Y. Song, J. Zhang, N. Z. Wang, Z. Sun, Y. Yi, Y. Z. Wu, S. Wu, J. Zhu *et al.*, *Nature*, 2018, **563**, 94–99.
9 M. Gibertini, M. Koperski, A. Morpurgo and K. Novoselov, *Nature nanotechnology*, 2019, **14**, 408–419.
10 C. Gong and X. Zhang, *Science*, 2019, **363**, eaav4450.
11 J. L. Lado and J. Fernández-Rossier, *2D Materials*, 2017, **4**, 035002.
12 J. Liu, M. Shi, J. Lu and M. Anantram, *Physical Review B*, 2018, **97**, 054416.
13 B. Huang, G. Clark, E. Navarro-Moratalla, D. R. Klein, R. Cheng, K. L. Seyler, D. Zhong, E. Schmidgall, M. A. McGuire, D. H. Cobden *et al.*, *Nature*, 2017, **546**, 270–273.
14 W.-B. Zhang, Q. Qu, P. Zhu and C.-H. Lam, *Journal of Materials Chemistry C*, 2015, **3**, 12457–12468.
15 M. A. McGuire, H. Dixit, V. R. Cooper and B. C. Sales, *Chemistry of Materials*, 2015, **27**, 612–620.
16 T. Song, M. W.-Y. Tu, C. Carnahan, X. Cai, T. Taniguchi,

View Article Online
DOI: 10.1039/D0TC03147J

K. Watanabe, M. A. McGuire, D. H. Cobden, D. Xiao, W. Yao *et al.*, *Nano letters*, 2019, **19**, 915–920.
17 Z. Zhu, Y. Cheng and U. Schwingenschlögl, *Physical Review B*, 2011, **84**, 153402.
18 G.-B. Liu, D. Xiao, Y. Yao, X. Xu and W. Yao, *Chemical Society Reviews*, 2015, **44**, 2643–2663.
19 Q. H. Wang, K. Kalantar-Zadeh, A. Kis, J. N. Coleman and M. S. Strano, *Nature nanotechnology*, 2012, **7**, 699.
20 D. J. O'Hara, T. Zhu, A. H. Trout, A. S. Ahmed, Y. K. Luo, C. H. Lee, M. R. Brenner, S. Rajan, J. A. Gupta, D. W. McComb *et al.*, *Nano letters*, 2018, **18**, 3125–3131.
21 X. Ma, T. Dai, S. Dang, S. Kang, X. Chen, W. Zhou, G. Wang, H. Li, P. Hu, Z. He *et al.*, *ACS applied materials & interfaces*, 2019, **11**, 10729–10735.
22 M. Bonilla, S. Kolekar, Y. Ma, H. C. Diaz, V. Kalappattil, R. Das, T. Eggers, H. R. Gutierrez, M.-H. Phan and M. Batzill, *Nature nanotechnology*, 2018, **13**, 289–293.
23 W. Cui, S. Xu, B. Yan, Z. Guo, Q. Xu, B. G. Sumpter, J. Huang, S. Yin, H. Zhao and Y. Wang, *Advanced Electronic Materials*, 2017, **3**, 1700024.
24 H. Wang, C. Li, P. Fang, Z. Zhang and J. Z. Zhang, *Chemical Society Reviews*, 2018, **47**, 6101–6127.
25 S. Imani Yengejeh, J. Liu, S. A. Kazemi, W. Wen and Y. Wang, *ACS omega*, 2020, **5**, 5994–6002.
26 H. Yuan, M. S. Bahramy, K. Morimoto, S. Wu, K. Nomura, B.-J. Yang, H. Shimotani, R. Suzuki, M. Toh, C. Kloc *et al.*, *Nature Physics*, 2013, **9**, 563–569.
27 S. Wu, J. S. Ross, G.-B. Liu, G. Aivazian, A. Jones, Z. Fei, W. Zhu, D. Xiao, W. Yao, D. Cobden *et al.*, *Nature Physics*, 2013, **9**, 149–153.
28 Y. Cheng, Z. Zhu, M. Tahir and U. Schwingenschlögl, *EPL (Europhysics Letters)*, 2013, **102**, 57001.
29 A.-Y. Lu, H. Zhu, J. Xiao, C.-P. Chuu, Y. Han, M.-H. Chiu, C.-C. Cheng, C.-W. Yang, K.-H. Wei, Y. Yang *et al.*, *Nature nanotechnology*, 2017, **12**, 744–749.
30 J. He and S. Li, *Computational Materials Science*, 2018, **152**, 151–157.
31 V. N. Strocov, M. Shi, M. Kobayashi, C. Monney, X. Wang, J. Krempasky, T. Schmitt, L. Patthey, H. Berger and P. Blaha, *Physical review letters*, 2012, **109**, 086401.
32 J. Li, B. Zhao, P. Chen, R. Wu, B. Li, Q. Xia, G. Guo, J. Luo, K. Zang, Z. Zhang *et al.*, *Advanced Materials*, 2018, **30**, 1801043.
33 M. Esters, R. G. Hennig and D. C. Johnson, *Physical Review B*, 2017, **96**, 235147.
34 M. Kan, B. Wang, Y. H. Lee and Q. Sun, *Nano Research*, 2015, **8**, 1348–1356.
35 N. Luo, C. Si and W. Duan, *Physical Review B*, 2017, **95**, 205432.
36 H. Zhang, L.-M. Liu and W.-M. Lau, *Journal of Materials Chemistry A*, 2013, **1**, 10821–10828.
37 C. Van Bruggen and C. Haas, *Solid State Communications*, 1976, **20**, 251–254.
38 P. M. Coelho, K. Nguyen Cong, M. Bonilla, S. Kolekar, M.-H. Phan, J. Avila, M. C. Asensio, I. I. Oleynik and M. Batzill, *The Journal of Physical Chemistry C*, 2019, **123**, 14089–14096.
39 Z. Popov, N. Mikhaleva, M. Visotin, A. Kuzubov, S. Entani, H. Naramoto, S. Sakai, P. Sorokin and P. Avramov, *Physical Chemistry Chemical Physics*, 2016, **18**, 33047–33052.
40 J. Zhou, J. Qiao, C.-G. Duan, A. Bournel, K. L. Wang and W. Zhao, *ACS applied materials & interfaces*, 2019, **11**, 17647–17653.
41 H.-R. Fuh, C.-R. Chang, Y.-K. Wang, R. F. Evans, R. W. Chantrell and H.-T. Jeng, *Scientific reports*, 2016, **6**, 32625.
42 J. M. Soler, E. Artacho, J. D. Gale, A. García, J. Junquera, P. Ordejón and D. Sánchez-Portal, *Journal of Physics: Condensed Matter*, 2002, **14**, 2745.
43 N. Troullier and J. L. Martins, *Physical review B*, 1991, **43**, 1993.
44 C. Zhang, Y. Nie, S. Sanvito and A. Du, *Nano letters*, 2019, **19**, 1366–1370.
45 J. Yang, A. Wang, S. Zhang, J. Liu, Z. Zhong and L. Chen, *Physical Chemistry Chemical Physics*, 2019, **21**, 132–136.
46 H.-R. Fuh, B. Yan, S.-C. Wu, C. Felser and C.-R. Chang, *New Journal of Physics*, 2016, **18**, 113038.
47 S. Dudarev, G. Botton, S. Savrasov, C. Humphreys and A. Sutton, *Physical Review B*, 1998, **57**, 1505.
48 W. Yu, J. Li, T. S. Herng, Z. Wang, X. Zhao, X. Chi, W. Fu, I. Abdelwahab, J. Zhou, J. Dan *et al.*, *Advanced Materials*, 2019, **31**, 1903779.
49 L. Webster, L. Liang and J.-A. Yan, *Physical Chemistry Chemical Physics*, 2018, **20**, 23546–23555.
50 B. Huang, J. Cenker, X. Zhang, E. L. Ray, T. Song, T. Taniguchi, K. Watanabe, M. A. McGuire, D. Xiao and X. Xu, *Nature Nanotechnology*, 2020, 1–5.
51 E. B. Isaacs and C. A. Marianetti, *Physical Review B*, 2016, **94**, 035120.
52 G. Duvjir, B. K. Choi, I. Jang, S. Ulstrup, S. Kang, T. Thi Ly, S. Kim, Y. H. Choi, C. Jozwiak, A. Bostwick *et al.*, *Nano letters*, 2018, **18**, 5432–5438.
53 J. Zhang, J. M. Soon, K. P. Loh, J. Yin, J. Ding, M. B. Sullivian and P. Wu, *Nano letters*, 2007, **7**, 2370–2376.
54 J. Kanamori, *Journal of Applied Physics*, 1960, **31**, S14–S23.
55 J. B. Goodenough, *Physical Review*, 1955, **100**, 564.
56 C. Huang, Y. Du, H. Wu, H. Xiang, K. Deng and E. Kan, *Physical review letters*, 2018, **120**, 147601.
57 S. Blügel and G. Bihlmayer, *Magnetism of Low-Dimensional Systems: Theory in Handbook of Magnetism and Advanced Magnetic Materials, ed. by H. Kronmüller and S. Parkin*, 2007.
58 Y. Ma, Y. Dai, M. Guo, C. Niu, Y. Zhu and B. Huang, *ACS nano*, 2012, **6**, 1695–1701.
59 Y. Zhou, Z. Wang, P. Yang, X. Zu, L. Yang, X. Sun and F. Gao, *Acs Nano*, 2012, **6**, 9727–9736.
60 Y. Ma, Y. Dai, M. Guo, C. Niu, L. Yu and B. Huang, *Nanoscale*, 2011, **3**, 2301–2306.
61 S.-C. Lee, K.-S. Kim, S.-H. Lee, U.-H. Pi, K. Kim, Y. Jang and U.-I. Chung, *Journal of Applied Physics*, 2013, **113**, 023914.
62 Y. Yue, *Journal of Superconductivity and Novel Magnetism*, 2017, **30**, 1201–1206.
63 R. Albaridy, A. Manchon and U. Schwingenschlögl, *Journal of Physics: Condensed Matter*, 2020, **32**, 355702.
64 V. Berezinsky, *Zh. Eksp. Teor. Fiz.*, 1970, **32**, 493–500.
65 J. M. Kosterlitz and D. J. Thouless, *Journal of Physics C: Solid State Physics*, 1973, **6**, 1181.
66 J. F. Fernández, M. F. Ferreira and J. Stankiewicz, *Physical Review B*, 1986, **34**, 292.
67 J. Zeng, E. Liu, Y. Fu, Z. Chen, C. Pan, C. Wang, M. Wang, Y. Wang, K. Xu, S. Cai *et al.*, *Nano letters*, 2018, **18**, 1410–1415.
68 M. Cui, Y. Guo, Y. Zhu, H. Liu, W. Wen, J. Wu, L. Cheng, Q. Zeng and L. Xie, *The Journal of Physical Chemistry C*, 2018,

View Article Online
DOI: 10.1039/D0TC03147J

122, 7551–7556.

69 H. Xiang, B. Xu, Y. Xia, J. Yin and Z. Liu, *Scientific reports*, 2016, **6**, 1–8.

70 J. Liu, W.-J. Hou, C. Cheng, H.-X. Fu, J.-T. Sun and S. Meng, *Journal of Physics: Condensed Matter*, 2017, **29**, 255501.

71 S. Y. Park, D. S. Kim, Y. Liu, J. Hwang, Y. Kim, W. Kim, J.-Y. Kim, C. Petrovic, C. Hwang, S.-K. Mo *et al.*, *Nano letters*, 2019, **20**, 95–100.

72 X. Li, X. Wu, Z. Li, J. Yang and J. Hou, *Nanoscale*, 2012, **4**, 5680–5685.

73 S. Grimme, J. Antony, S. Ehrlich and H. Krieg, *The Journal of chemical physics*, 2010, **132**, 154104.

74 Z. Zhang, X. Ni, H. Huang, L. Hu and F. Liu, *Physical Review B*, 2019, **99**, 115441.